Chemical
Science

ROYAL SOCIETY
OF CHEMISTRY

EDGE ARTICLE

View Article Online
View Journal | View Issue

Cite this: *Chem. Sci.*, 2025, **16**, 6376

All publication charges for this article have been paid for by the Royal Society of Chemistry

Received 8th January 2025
Accepted 3rd March 2025

DOI: 10.1039/d5sc00156k

rsc.li/chemical-science

Near-infrared light-activatable iridium(III) complexes for synergistic photodynamic and photochemotherapy†

Monika Negi and V. Venkatesh *

Near-infrared (NIR) light-activatable photosensitizers (PSs) have garnered tremendous interest as PSs for photodynamic therapy (PDT) due to the deeper tissue penetration ability and lower toxicity of NIR radiation. However, the low reactive oxygen species (ROS) production, poor tumor accumulation, and residual toxicity of these PSs pose major challenges for further development in this regime. In this regard, we have meticulously designed and synthesized two novel mitochondria-targeting iridium(III)–dithiocarbamate–cyanine complexes, Ir1@hcy and Ir2@hcy. In particular, Ir2@hcy exhibited both type I and type II PDT with excellent singlet oxygen ($^1O_2$) and hydroxyl radical ($^•OH$) generation ability under 637 nm/808 nm irradiation, even at an ultra-low power intensity (2 mW cm^{-2}). Under higher-power irradiation (100 mW cm^{-2}), the reactive oxygen species (ROS) production by Ir2@hcy was augmented. The elevated levels of ROS caused the disintegration of Ir2@hcy to produce cytotoxic oxindole scaffolds through the dioxetane mechanism. The synergistic production of ROS and cytotoxic species effectively induced mitochondria-mediated cancer cell death in both *in vitro* and 3D tumor spheroid models, offering a new avenue to develop combinational phototherapy (PDT + PACT) for cancer treatment with spatio-temporal precision.

Introduction

Photodynamic therapy (PDT) has gained considerable attention as a non-invasive treatment strategy with high spatio-temporal precession and painless treatment procedures.[1–3] During the PDT process, photosensitizers (PSs) generate cytotoxic reactive oxygen species (ROS) *via* electron transfer (type I PDT) or energy transfer (type II PDT) upon light exposure, which can induce the apoptosis or necrosis of cancer cells.[4,5] Photolabile complexes, which release cytotoxic metal complexes or ligands after light irradiation, are categorized as potential candidates for photo-activated chemotherapy (PACT).[6,7] Some ruthenium (Ru)- and platinum (Pt)-based complexes have been reported to achieve synergistic therapeutic efficiency by uncaging cytotoxic complexes and ligands after light exposure.[8,9] However, photolabile iridium complexes have yet to be explored in PACT with PDT.

Near-infrared (NIR) PSs exhibiting type I and type II PDT are highly sought after due to the synergistic enhancement in ROS production, which further overcomes oxygen dependence for their mode of action. However, most of the reported PSs (including FDA-approved PSs) and photolabile complexes are activated by UV-visible light (365–700 nm), which restricts their clinical utility in treating deep-seated tumours by affecting their penetration depth due to the higher scattering and strong absorption of visible light by tissues.[10–12] In contrast, PSs activated by NIR light fall in the phototherapeutic window (700–900 nm), which penetrates deeper into tissues with low absorption and scattering properties.[13,14] Metal complex-based PSs have several advantages, such as high triplet sensitization, better cellular uptake, and improved solubility compared to their organic counterparts.[15] To date, NIR-active metal complex-based PSs are scarce. Hence, there is an urgent need for the development of NIR-active metal complex-based PSs exhibiting both type I and type II PDT.

To address these concerns, considerable efforts have been put forth toward developing PSs that combine metal complexes and organic fluorophores with good photophysical properties. For example, xanthene,[16] coumarin,[17] boron dipyrromethene (BODIPY),[18] cyanine,[19] Nile red,[20] porphyrin,[21] and phthalocyanine[22] conjugates with various transition metals, such as iridium, platinum, and ruthenium, have been reported. Various cyanine scaffolds have been explored in different biological applications, such as *in vivo* photoacoustic imaging, type II PDT treatment, pH sensing, and GSH sensing.[23,24] The FDA approved dye indocyanine green (ICG) is clinically utilized as an intra-operative imaging agent.[25] Heptamethine cyanine (hcy) derivatives exhibit a high molar extinction coefficient in the NIR region, adaptable properties, and structural flexibility. Recently, Peng *et al.* incorporated heavy atoms such as sulfur and selenium into the hcy scaffold for efficient type II PDT (Fig. 1a).[26] The heavy atom effect

---

Department of Chemistry, Indian Institute of Technology Roorkee, Roorkee 247667, Uttarakhand, India. E-mail: venkatesh.v@cy.iitr.ac.in

† Electronic supplementary information (ESI) available. See DOI: https://doi.org/10.1039/d5sc00156k

of transition metals, such as iridium and ruthenium also involves spin–orbit coupling, and intramolecular charge transfer (ICT) between metal and hcy efficiently leads to higher triplet sensitization. S. Yang and co-workers recently utilized iridium(III)–cyanine conjugate-based nanoparticles for *in vivo* photoacoustic image-guided type II PDT applications.[27] However, the exploitation of self-degradable iridium(III) complexes as type I and II PSs remain unexplored. In 2022, Chan *et al.* employed the concept of repurposing the photoinstability of hcy scaffolds through the dioxetane mechanism for *in vivo* delivery (Fig. 1b).[28] Notably, most traditional organic and inorganic PSs are non-biodegradable, which causes their undesirable side effects post-treatment. Specifically, the residual PSs, upon exposure to sunlight, produce toxic ROS and damage normal cells *in vivo*.[29] Additionally, few organic and polymer-conjugated PSs that can self-degrade after PDT treatment have been reported.[30] Hence, it is of great significance to develop self-degradable metal complex-based PSs for efficient type I and II PDT that avoid post-treatment complications by degrading into cytotoxic species for synergistic therapeutic efficacy.

In this work, two novel iridium(III)–dithiocarbamate complexes decorated with an hcy unit were synthesized using different C^N ligands. The piperazine unit serves as a bridge between the metal center and the electron-withdrawing cyanine system. Interestingly, the synthesized complex could be activated with ultra-low power NIR light, generating $^1O_2$ and $^{\bullet}OH$ for type I and II PDT, respectively. Concurrently, at high laser power, the produced ROS induced dioxetane formation followed by ligand degradation through ring opening, thus providing a new platform to deliver cytotoxic oxindole derivatives. The positive charge on their scaffold facilitated their accumulation in the mitochondria of cancer cells. The NIR-responsive ROS generation and release of cytotoxic species induced cancer cell death by amplifying oxidative stress (Fig. 1c). This strategy could potentially revolutionize cancer treatment through its organelle-targeted type I and II PDT effect and self-degradable properties with PACT, which offer a promising solution to reduce the risk of long-term side effects and instill confidence in its clinical translation.

Results and discussion

Synthesis and characterization

We first synthesized a cyanine-based NIR-activatable photosensitive ligand (compound **3**). Previous studies have

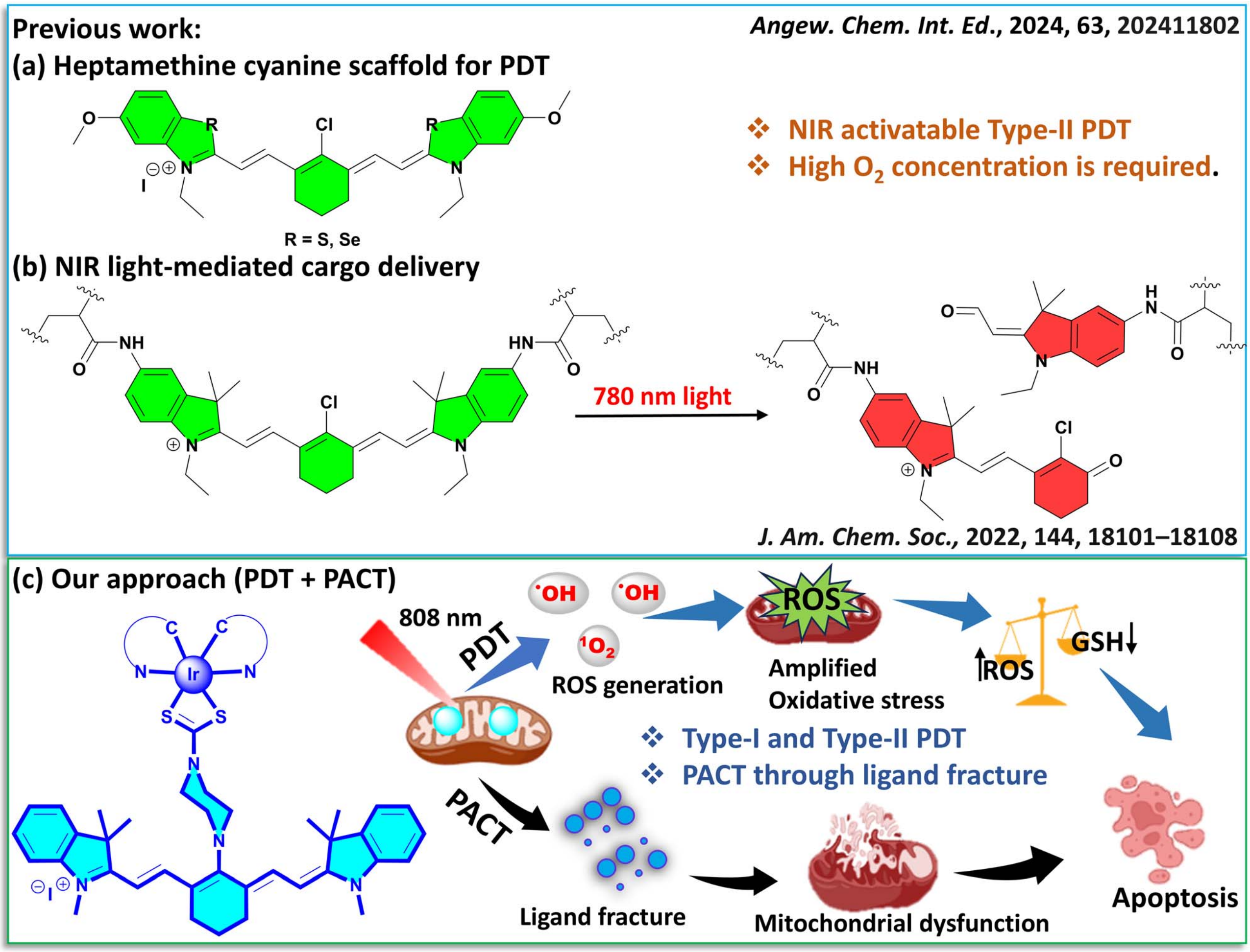

Fig. 1 (a) Reported hcy scaffolds as type II PDT agents. (b) Photolysis property of hcy under NIR light. (c) Our PDT/PACT approach using iridium(III)–dithiocarbamate–cyanine complexes.

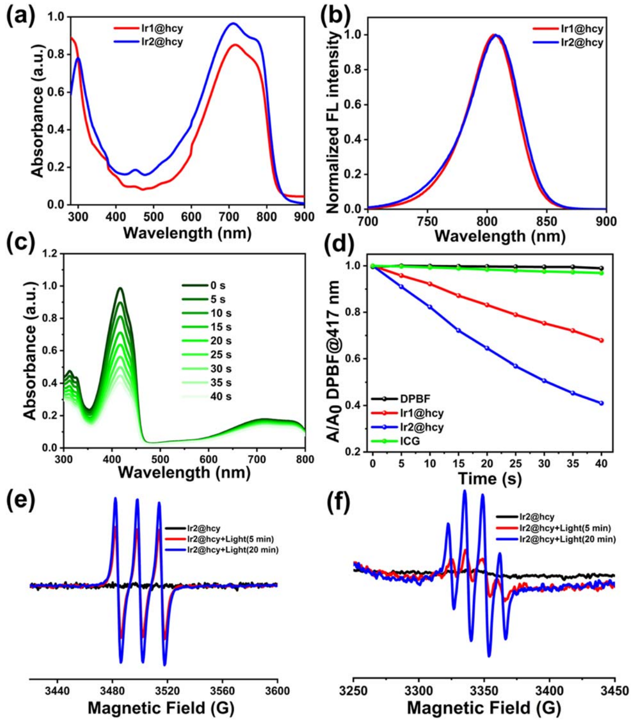

Fig. 2 (a) Absorption and (b) emission spectra of the iridium(III)–dithiocarbamate–cyanine complexes (10 μM) in DMSO. (c) DPBF degradation in the presence of Ir2@hcy at different intervals of light irradiation. (d) Normalized DPBF absorption change for the complexes and references under light irradiation. (e) TEMP–$^1O_2$ and (f) DMPO–$^{\bullet}OH$ adduct formation for Ir2@hcy after light irradiation.

demonstrated that the PDT efficiency of organic PSs could be improved by incorporating transition metals into the system.[31] Encouraged by this, we linked compound **3** with an iridium complex through a piperazine bridge with the aim of obtaining a NIR-activatable iridium complex with improved photosensitization ability. Firstly, compounds **1** and **2** were synthesized using 2,3,3-trimethyl-3*H*-indole and cyclohexanone as starting materials, respectively. Following this, compound **3** was synthesized chemically *via* Knoevenagel condensation using compounds **1** and **2**. Subsequently, piperazine was used as a precursor to synthesize compound **4**, with the disubstituted compound being obtained as a byproduct. The iridium dimers *i.e.* [(ppy)$_2$-Ir-μ-Cl]$_2$ (denoted as ppy dimer) and [(thpy)$_2$-Ir-μ-Cl]$_2$ (denoted as thpy dimer), were then reacted with 10 equivalents of compound **4** (without purification) to the form iridium(III)–dithiocarbamate complexes (compound **5** and **6**), rather than the binuclear iridium(III)–dithiocarbamate complexes. Finally, the synthesized metal complexes **5** and **6** were reacted with compound **3** in the presence of NEt$_3$ and DMF under an inert atmosphere at 95 °C to produce two [Ir(C^N)$_2$(S^S)] iridium(III)–dithiocarbamate–cyanine complexes, *i.e.*, Ir1@hcy and Ir2@hcy (Scheme 1). The products were isolated through column chromatography. The detailed synthetic procedures are described in the ESI.† The synthesized ligands and complexes were characterized using ^{1}H NMR, ^{13}C NMR, electrospray ionization high-resolution mass spectrometry (ESI-HRMS) and high-performance liquid chromatography (HPLC) (Fig. S1–S17†). The UV-vis-NIR absorption spectra revealed two strong NIR absorption maxima (λ_{abs}) at 715 nm and 770 nm in DMSO, demonstrating the incorporation of the cyanine moiety (Fig. 2a). Additionally, both complexes exhibited a ligand-centered ($^1\pi$–π^*) transition at 280–300 nm, and broad absorption bands (less intense) at ∼450 nm attributed to metal-to-ligand charge transfer (MLCT). Additionally, the fluorescence (FL) spectra of both complexes were recorded in DMSO (Fig. 2b) and showed a maximum NIR fluorescence emission at 810 nm with an excitation wavelength of 765 nm (Stokes shift ∼45 nm). The relative fluorescence quantum yields (ϕ_f) of Ir1@hcy and Ir2@hcy were measured to be 12.74% and 11.01% in DMSO using ICG as the reference ($\phi_f = 14.3\%$ in DMSO). The synthesized complexes showed excellent stability in the dark for 48 h in a DMSO/PBS (<0.5%) solution (Fig. S18a and b†). Moreover, no significant change in absorption was observed after ultra-low-power light irradiation (637 nm or 808 nm, 2 mW cm^{-2}) for 30 min, demonstrating their potential to act as efficient PSs (Fig. S18c†). However, Ir1@hcy and Ir2@hcy showed considerable absorbance changes after being irradiated with a high-

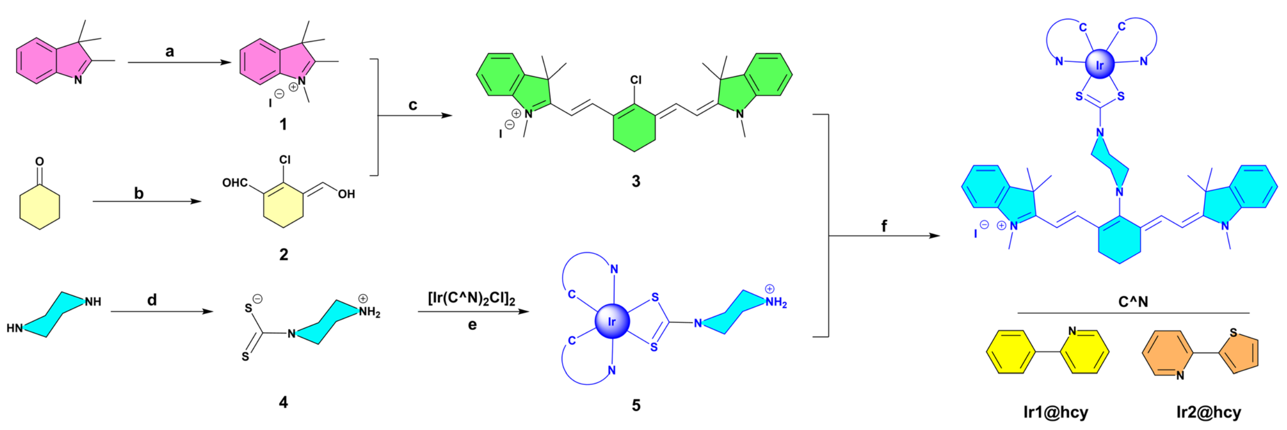

Scheme 1 General reaction scheme of the synthesis of NIR-active iridium(III)–dithiocarbamate–cyanine complexes investigated in this study. Reaction conditions: (a) MeI, MeCN, reflux, 12 h; (b) POCl$_3$, DMF, 80 °C, 5 h; (c) acetic anhy., NaOAc, N$_2$ atm., 130 °C, 2 h; (d) CS$_2$, H$_2$O, 25 °C, 10 min; (e) Na$_2$CO$_3$, DCM, 25 °C, 12 h; (f) NEt$_3$, DMF, 95 °C, 12 h.

power laser source (808 nm, 100 mW cm^{-2}) for 30 min (Fig. S18d†). The significant photodegradation of both complexes under a higher-power-density light source, as evidenced by the disappearance of the NIR absorption band, is consistent with the previously reported self-degradation properties of the hcy scaffold. The photodegradation of both complexes was greater than that of the cyanine–piperazine (hcy–pip) ligand (synthesized for comparison) under identical conditions, confirming the influence of the metal center.

Furthermore, we tested the $^1O_2$ generation of the synthesized Ir(III)–dithiocarbamate–cyanine complexes under an ultra-low-power source (808 nm, 2 mW cm^{-2}) using 1,3-diphenylisobenzofuran (DPBF) as an $^1O_2$ indicator. Interestingly, the singlet oxygen quantum yield (ϕ_Δ) values for Ir1@hcy and Ir2@hcy were ~10.1 and ~18.8 times greater than that of ICG (reference) (Fig. 2c and d). These characteristics were not exhibited by the hcy–pip ligand alone (Fig. S19†). To further verify the generation of different ROS, a more reliable technique, namely, electron paramagnetic resonance (EPR) analysis, was conducted using 2,2,6,6-tetramethylpiperidine (TEMP, $^1O_2$ trapping agent) and 5,5-dimethyl-1-pyrroline *N*-oxide (DMPO, $^{\bullet}OH$ trapping agent) in acetonitrile. After 700 nm laser irradiation for 5 min, the solutions of Ir2@hcy and TEMP–$^1O_2$ adduct showed a characteristic three-line EPR signal with equal intensities (1 : 1 : 1) (Fig. 2e). Similarly, a four-line spectrum with 1 : 2 : 2 : 1 intensity was observed when DMPO was used to detect hydroxyl radicals ($^{\bullet}OH$) (Fig. 2f). Furthermore, no apparent EPR signals were observed under dark conditions. The bridging unit, piperazine, also facilitates the generation of various ROS *via* long-range electron transfer.[32,33] These results demonstrated that the synthesized complex could efficiently generate $^1O_2$ and $^{\bullet}OH$ at a very low power density and had self-degradation properties under high-power light irradiation.

Under higher power laser irradiation (808 nm, 100 mW cm^{-2}), the generated ROS ($^1O_2$ and $^{\bullet}OH$) degrade Ir2@hcy to produce various oxindole derivatives through the dioxetane intermediate. In brief, the excited Ir2@hcy reacts with the produced $^1O_2$ to form a dioxetane intermediate. This unstable intermediate decomposes to form various oxindole derivatives (Scheme 2). We employed the ESI-HRMS technique after light irradiation to verify this mechanism. The peak with an *m*/*z* corresponding to the Ir2@hcy complex was not found in the solution after 30 min of irradiation by an 808 nm laser. Moreover, peaks corresponding to oxindole derivatives and indole-based species were observed at *m*/*z* 176.1074 and 202.1275 (Fig. S20†).

Cellular localization and *in vitro* photocytotoxicity

The cellular internalization and localization of a PS are crucial for effective PDT treatment. The cellular uptake of Ir2@hcy in human melanoma (A375) cells was visualized using a fluorescence microscope (FM). The results showed a homogeneous distribution of red fluorescence inside the cells within 30 min that gradually increased with incubation time, confirming its efficient internalization (Fig. S21†). Both compounds tend to aggregate in polar solvents such as water, which is in agreement with previous reports in the literature on cyanine-based scaffolds.[34–36] Most cyanine derivatives show cytoselective effects against cancer cells, and hence, they have been explored as anticancer agents due to their tumour-targeting ability.[37–39] Thus, the lipophilicity of the synthesized compounds was determined by measuring the distribution of the complexes between octanol and water. As

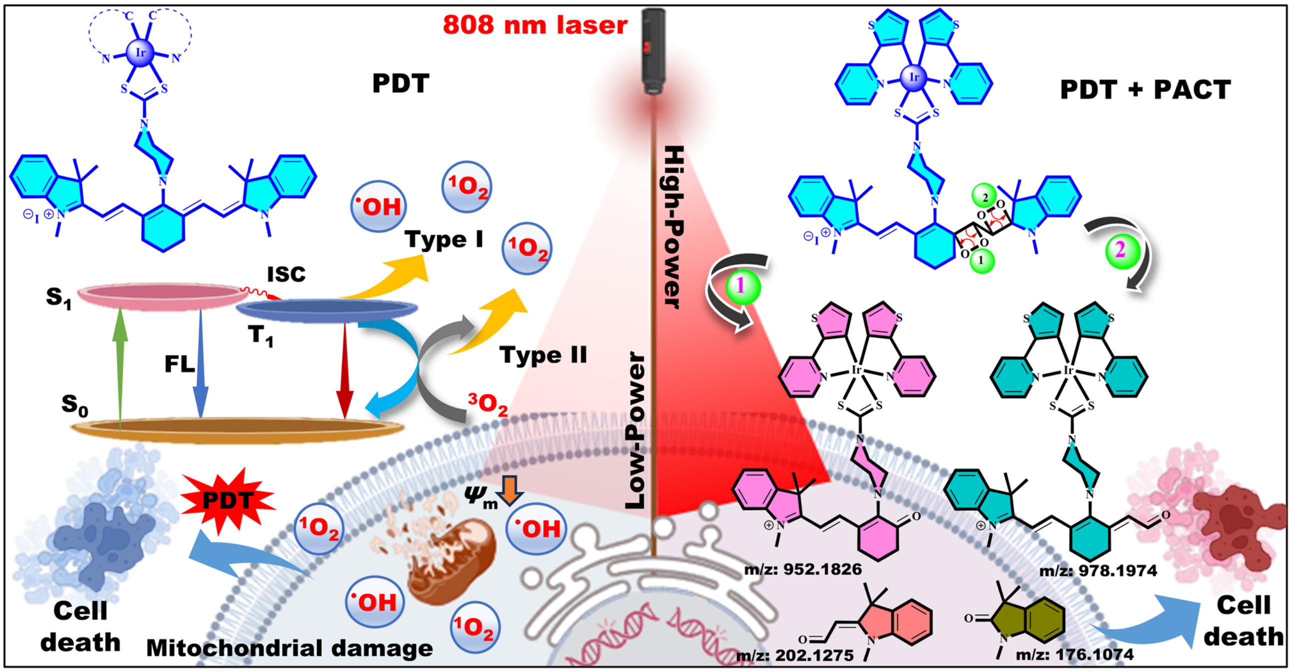

Scheme 2 Schematic illustration of NIR-active iridium(III)–dithiocarbamate–cyanine complexes exhibiting type I and type II PDT at lower irradiation power to elicit PDT, and self-degradation of Ir2@hcy at high laser power to produce cytotoxic oxindole and indole derivatives for PACT.

shown in Table S1,† the log *P* value of Ir2@hcy (1.74) was higher than that of Ir1@hcy (0.65), suggesting enhanced cellular accumulation in tumour cells, which correlates well with the fluorescence uptake studies performed on A375 cells after 30 min of treatment. The cellular accumulation and distribution of Ir2@hcy in the A375 cells in terms of Ir was measured using ICP-MS. As shown in Fig. S22,† the Ir content was higher in the mitochondria than in the cytosol within 1 h of incubation, suggesting its mitochondrial targeting ability due to the lipophilic cations of the quaternary ammonium salt moiety in its scaffold.[40] Moreover, the uptake of Ir2@hcy was statistically different at 37 °C and 4 °C, which suggested that intracellular Ir2@hcy accumulation occurred mainly through an energy-dependent pathway (Fig. S23†). Simultaneously, the intracellular co-localization of Ir2@hcy was evaluated using commercially available organelle-selective dyes, *i.e.*, Mitotracker Green (MTG), nuclear staining dye (DAPI) and Lysotracker green (LTG). As expected, the signal of Ir2@hcy predominantly overlapped with the MTG signal in the mitochondria with a high Pearson's correlation coefficient (*P*) value of 0.93 (Fig. 3a) due to the intrinsic positive charge within the system. In contrast, the *P* values of Ir2@hcy with the Lysotracker and DAPI signals were only 0.62 and 0.40, respectively (Fig. 3a and S24†). These findings indicate that the Ir2@hcy complex is primarily localized in mitochondria due to the more negative membrane potential of mitochondria in cancer cells. Under PDT, mitochondria-targeting PSs can rapidly alter the biological functions of various organelles, leading to cancer cell death.

The mechanism of action for PDT activity includes elevated ROS levels in the cells. *In vitro* ROS generation by Ir2@hcy was evaluated using cell-permeable 2′,7′-dichlorodihydro fluorescein diacetate (DCFH-DA), a ROS probe. DCFH-DA is oxidized by different ROS to convert it into its green-fluorescent derivative 2′,7′-dichlorofluorescein (DCF). For this, cells were treated with Ir2@hcy (5 μM) for 1 h and then exposed to light or maintained in the dark for 10 min. The FM images under the green channel showed intense green fluorescence from DCF in cells treated with Ir2@hcy followed by light irradiation, indicating significant ROS generation through PDT activity. In contrast, almost negligible green fluorescence was observed in the control, Ir2@hcy-alone, and light-alone groups (Fig. 3b). Furthermore, the fluorescence quantification studies showed a 10-fold increase in ROS level compared to control cells, which confirms the elevated level of ROS after photoactivation of Ir2@hcy (Fig. 3c).

Encouraged by their efficient *in vitro* ROS production and photodegradation ability of the complexes, we investigated their *in vitro* photo-cytotoxicity index (PI) using the standard 3-(4,5-dimethylthiazol-2-yl)-2,5-diphenyltetrazolium bromide (MTT) assay in a concentration-dependent manner. The results revealed that the synthesized complexes exhibited low dark toxicity ($IC_{50} \sim 20$ μM) toward the human melanoma (A375), lung adenocarcinoma (A549), and human colorectal carcinoma (HCT116) cell lines (Table S2†). After low-power red light irradiation (637 nm, 2 mW cm^{-2}, 20 min), Ir2@hcy exhibited high photocytotoxicity ($IC_{50} = 0.069$ μM with PI = 188) towards the A375 cell line, demonstrating severe damage to cancer cells through type I and type II PDT. Furthermore, when the power density was increased to 20 mW cm^{-2}, the cell viability was drastically reduced ($IC_{50} = 0.015$ μM with PI = 866) due to the synergistic effect of PDT and PACT (Fig. 3d, S25a, b and d†). Various 3,3-disubstituted oxindoles have shown promising biological activities, such as anti-cancer, kinase inhibition, and anti-angiogenesis activities.[41–44] Hence, the greater cytotoxicity could be due to the release of oxindole moieties. Additionally, none of the complexes resulted in a significant reduction in cell viability in the normal embryonic kidney cell line (HEK293), suggesting their remarkable biocompatibility with this normal cell line (Fig. S25c†). A possible reason for this selectivity is the better uptake efficiency of Ir2@hcy in cancerous cells. The decrease in the IC_{50} value with increasing power density confirms the degradation of Ir2@hcy due to greater ROS generation (Fig. S26†). Cell viability studies of both complexes showed similar phototoxicity under the 800 nm laser setup within 5 min of exposure (Fig. S27†). Disruption and alterations in cellular morphology also accompanied the high photocytotoxicity of the Ir2@hcy + light group (Fig. S28†). Compared to the control groups, compromised cell membrane integrity, cell detachment, cell shrinkage, and membrane blebbing were observed in Ir2@hcy-mediated PDT, followed by PACT.

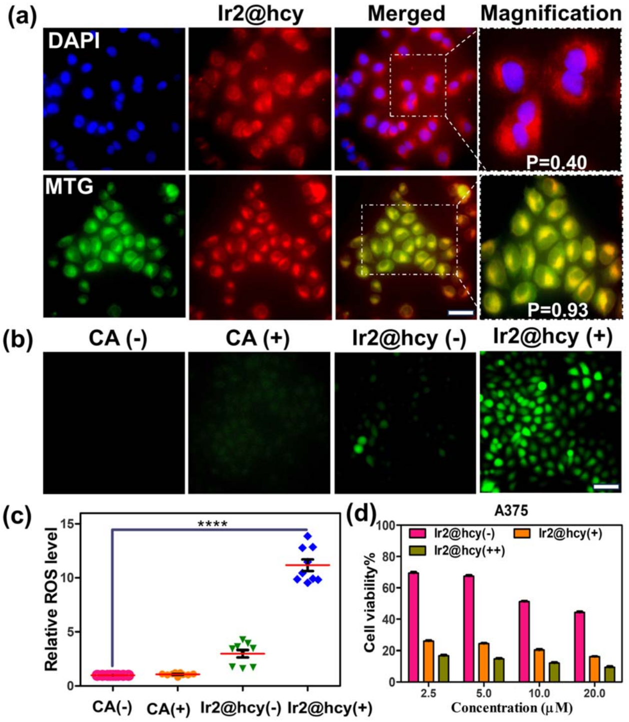

Fig. 3 (a) Intracellular localization of Ir2@hcy with organelle trackers in A375 cells. Magnification: 60×, scale bar: 20 μm. (b) Intracellular ROS detection in A375 cells using the probe DCFH-DA. Magnification: 40×, scale bar: 20 μm. (c) Quantification of intracellular ROS levels for different groups. Data represented as mean ± S.D. One-way ANOVA test, $n = 9$, $****p < 0.0001$. (d) Cell viability of A375 cells incubated with Ir2@hcy after light irradiation for 20 min (CA represents cells without any treatment, "+" represents with light, and "−" represents without light, and "++" represents high power density).

Mitochondrial dysfunction and spheroid studies

Mitochondrial membrane integrity plays a crucial role in eukaryotes for various cellular metabolism processes, such as

ATP production, the electron transport process, and cell death signaling.[45] Hence, the change in mitochondria membrane potential (MMP) was measured using mitochondria depolarization studies. The mitochondrial localization and intracellular ROS generation further motivated us to assess the destruction of the mitochondrial membrane using the dye JC-1. JC-1, a cationic dye, emits red fluorescence inside healthy and intact mitochondria, where it is present in an aggregated form. However, the JC-1 monomer emits green fluorescence for depolarized mitochondria. Fig. 4a shows the intense JC-1 monomer emission in the green channel for Ir2@hcy after light irradiation, which depicts mitochondrial membrane depolarization with the loss of MMP. In contrast, intact mitochondria were visualized in the red channel due to the JC-1 aggregates for the other control groups, indicating the absence of mitochondrial destruction. As Ir2@hcy also emits in the red channel, all the images were taken at different exposure times so that no disturbance would occur while performing the assay (Fig. S29†). These results suggest that the PDT activity of Ir2@hcy could potentially impair mitochondrial functions. Lowering the MMP ultimately leads to tumour cell ablation, which can be detected through live/dead cell staining using fluorescein diacetate (FDA) and propidium iodide (PI). FDA is a cell-permeable dye that shows green fluorescence in live cells, whereas PI is a cell-impermeable dye that intercalates with DNA to emit red fluorescence for dead cells. The results demonstrated that most cells showed intense red fluorescence from PI, which corresponds to dead cells, when incubated with Ir2@hcy followed by light exposure (Fig. S30†). The control groups revealed that both Ir2@hcy and 637 nm light irradiation are essential to induce cell death.

To mimic the tumour microenvironment, the PDT and PACT efficacy of Ir2@hcy were tested using three-dimensional A375 multicellular tumour spheroids (MCTSs). These MCTSs exhibit a hypoxic or necrotic core at the center, which experiences oxygen deprivation, low pH, and nutrient starvation.[46] A significant amount of Ir2@hcy complex was visualized at the periphery of the MCTS in the red channel by FM within 30 min of incubation (Fig. S31†).

Furthermore, the efficacy of Ir2@hcy in PDT and PACT in tumour spheroids was investigated using a live–dead co-staining assay with FDA/PI. The results were similar to the FDA/PI assay for the 2D monolayer cells. Notably, significant green FDA fluorescence is observed for all the control groups. However, most of the cells were stained with PI after light irradiation (Fig. 4b), demonstrating the dual role of PDT and PACT in effectively inducing cell death.

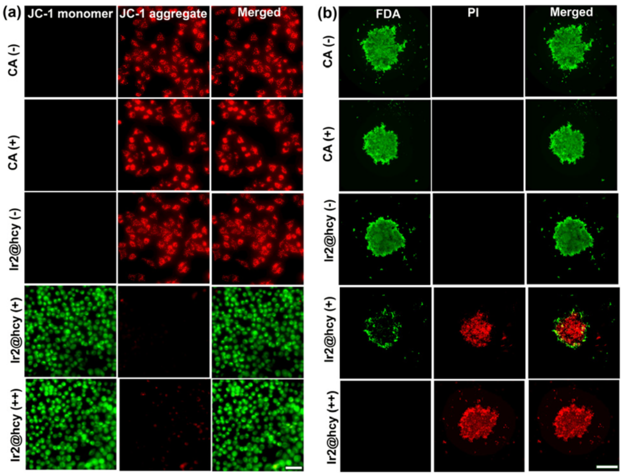

Fig. 4 (a) Mitochondrial membrane potential studies using the dye JC-1 in A375 cells for different groups. Magnification: 40×, scale bar: 20 μm (b) live/dead staining of A375 MCTSs using the dyes FDA and PI. Magnification: 4×, scale bar: 200 μm (CA represents cells without any treatment, "+" represents with light, "−" represents without light, and "++" represents high power density).

Conclusions

We have successfully synthesized two novel iridium(III)–dithiocarbamate complexes with a heptamethine cyanine unit to induce an ICT effect. Both complexes exhibited excellent NIR absorption and fluorescence emission. Complex Ir2@hcy exhibited a higher ϕ_Δ even at an ultra-low power density (808 nm, 2 mW cm^{-2}). Mitochondria-targeting Ir2@hcy generates intracellular ROS under low-power irradiation (637 nm, 2 mW cm^{-2}, 20 min) and exhibited a high phototoxicity index (PI = 188) towards A375 cells in a 2D monolayer and a 3D MCTS model. Under high-power laser intensity (808 nm, 100 mW cm^{-2}), along with the ROS production, the $^1O_2$-mediated degradation of Ir2@hcy to release cytotoxic oxindole moieties enhances the therapeutic efficacy and potentially reduces the side effects of PDT by degrading the residual PS. In essence, Ir2@hcy marks a breakthrough in the development of metal-based NIR PSs exhibiting efficient type I and II PDT along with PACT.

Data availability

The data supporting this article have been included as part of the ESI.†

Author contributions

V. V. and M. N. conceptualized and designed the study. M. N. synthesized and characterized the complexes and performed all biological studies. The manuscript was written through the contribution of all the authors.

Conflicts of interest

There are no conflicts to declare.

Acknowledgements

All authors acknowledge the Indian Institute of Technology (IIT) Roorkee (FIG-100855), India, for financial support. The authors thank Dr B. V. V. S. Pavan Kumar for giving access to their fluorescence microscope facility and Dr S. Pradhan for the 808 nm laser. We also acknowledge the Institute

Instrumentation Centre (IIC, IIT Roorkee) for EPR, the Centre for Nanotechnology, IIT Roorkee for HPLC, and DST-FIST for the NMR facility (SR/FST/CS-II/2018/72(C)).

Notes and references

1 X. Hou, Y. Tao, Y. Pang, X. Li, G. Jiang and Y. Liu, *Int. J. Cancer*, 2018, **143**, 3050–3060.

2 D. Dolmans, D. Fukumura and R. Jain, *Nat. Rev. Cancer*, 2003, **3**, 380–387.

3 N. Alvarez and A. Sevilla, *Int. J. Mol. Sci.*, 2024, **25**, 1023.

4 H. S. Jung, J. Han, H. Shi, S. Koo, H. Singh, H.-J. Kim, J. L. Sessler, J. Y. Lee, J.-H. Kim and J. S. Kim, *J. Am. Chem. Soc.*, 2017, **139**, 7595–7602.

5 J. Sun, X. Cai, C. Wang, K. Du, W. Chen, F. Feng and S. Wang, *J. Am. Chem. Soc.*, 2021, **143**, 868–878.

6 A. Notaro and G. Gasser, *Chem. Soc. Rev.*, 2017, **46**, 7317–7337.

7 N. J. Farrer, L. Salassa and P. J. Sadler, *Dalton Trans.*, 2009, 10690–10701.

8 S. Bonnet, *J. Am. Chem. Soc.*, 2023, **145**, 23397–23415.

9 V. E. Y. Lee, C. F. Chin and W. H. Ang, *Dalton Trans.*, 2019, **48**, 7388–7393.

10 E. Ruggiero, S. A. Castro, A. Habtemariam and L. Salassa, *Dalton Trans.*, 2016, **45**, 13012–13020.

11 J. Li, H. Duan and K. Pu, *Adv. Mater.*, 2019, **31**, 1901607.

12 J. D. Knoll, B. A. Albani and C. Turro, *Acc. Chem. Res.*, 2015, **48**, 2280–2287.

13 S. Son, J. Kim, J. Kim, B. Kim, J. Lee, Y. Kim, M. Li, H. Kang and J. S. Kim, *Chem. Soc. Rev.*, 2022, **51**, 8201–8215.

14 Y. Ma, J. Shang, L. Liu, M. Li, X. Xu, H. Cao, L. Xu, W. Sun, G. Song and X.-B. Zhang, *J. Am. Chem. Soc.*, 2023, **145**, 17881–17891.

15 K. Xiong, F. Wei, Y. Chen, L. Ji and H. Chao, *Small Methods*, 2023, **7**, 2201403.

16 Y. Wu, J. Wu and W.-Y. Wong, *Biomater. Sci.*, 2021, **9**, 4843–4853.

17 E. O. Forte, A. Rovira, M. L. Corrales, A. H. Garcia, F. J. Ballester, E. I. Garcia, M. J. Redondo, M. Bosch, S. Nonell, M. D. Santana, J. Ruiz, V. Marchan and G. Gasser, *Chem. Sci.*, 2023, **14**, 7170–7184.

18 B. Bertrand, K. Passador, C. Goze, F. Denat, E. Bodio and M. Salmain, *Coord. Chem. Rev.*, 2018, **358**, 108–124.

19 A. Gandioso, E. Izquierdo-García, P. Mesdom, P. Arnoux, N. Demeubayeva, P. Burckel, B. Saubaméa, M. Bosch, C. Frochot, V. Marchán and G. Gasser, *Chem.–Eur. J.*, 2023, **29**, e202301742.

20 P. Barretta, S. Scoditti, D. Belletto, F. Ponte, V. Vigna, G. Mazzone and E. Sicilia, *J. Comb. Chem.*, 2024, **45**, 2034–2041.

21 K. Ding, Y. Zhang, W. Si, X. Zhong, Y. Cai, J. Zou, J. Shao, Z. Yang and X. Dong, *ACS Appl. Mater. Interfaces*, 2018, **10**, 238–247.

22 J. Bonelli, E. Ortega-Forte, G. Vigueras, J. Follana-Berná, P. Ashoo, D. Abad-Montero, N. Isidro, M. López-Corrales, A. Hernández, J. Ortiz, E. Izquierdo-García, M. Bosch, J. Rocas, A. Sastre-Santos, J. Ruiz and V. Marchán, *ACS Appl. Mater. Interfaces*, 2024, **16**, 38916–38930.

23 A. P. Gorka, R. R. Nani and M. J. Schnermann, *Org. Biomol. Chem.*, 2015, **13**, 7584–7598.

24 W. Sun, S. Guo, C. Hu, J. Fan and X. Peng, *Chem. Rev.*, 2016, **116**, 7768–7817.

25 S. Zhu, R. Tian, A. L. Antaris, X. Chen and H. Dai, *Adv. Mater.*, 2019, **31**, 1900321.

26 W. Liu, S. He, X. Ma, C. Lv, H. Gu, J. Cao, J. Du, W. Sun, J. Fan and X. Peng, *Angew. Chem., Int. Ed.*, 2024, **63**, 202411802.

27 Q. Yang, H. Jin, Y. Gao, J. Lin, H. Yang and S. Yang, *ACS Appl. Mater. Interfaces*, 2019, **11**, 15417–15425.

28 R. T. Hernandez, M. C. Lee, A. K. Yadav and J. Chan, *J. Am. Chem. Soc.*, 2022, **144**, 18101–18108.

29 H. Huang, W. Xie, Q. Wan, L. Mao, D. Hu, H. Sun, X. Zhang and Y. Wei, *Adv. Sci.*, 2022, **9**, 2104101.

30 R. R. Allison, H. C. Mota and C. H. Sibata, *Photodiagnosis Photodyn. Ther.*, 2004, **1**, 263–277.

31 S. A. McFarland, A. Mandel, R. Dumoulin-White and G. Gasser, *Curr. Opin. Chem. Biol.*, 2020, **56**, 23–27.

32 L. Chen, S. Yan, W.-J. Guo, L. Qiao, X. Zhan, B. Liu and H.-Q. Peng, *Chem. Sci.*, 2024, **15**, 16059–16068.

33 W. Zhu, Z. Ding, S. Guo, W. Guo, S. Yan, B. Liu, H. Li, Z. Liu, B. Tang and H. Peng, *Small*, 2024, **20**, 2309424.

34 X. Zhao, H. Zhao, S. Wang, Z. Fan, Y. Ma, Y. Yin, W. Wang, R. Xi and M. A. Meng, *J. Am. Chem. Soc.*, 2021, **143**, 20828–20836.

35 M. Ogawa, N. Kosaka, P. Choyke and H. Kobayashi, *ACS Chem. Biol.*, 2009, **4**, 535–546.

36 A. Levitz, F. Marmarchi and M. Henary, *Photochem. Photobiol. Sci.*, 2018, **17**, 1409–1416.

37 S. Luo, E. Zhang, Y. Su, T. Cheng and C. Shi, *Biomaterials*, 2011, **32**, 7127–7138.

38 C. Shi, J. B. Wu and D. Pan, *J. Biomed. Opt.*, 2016, **21**, 50901.

39 E. Cooper, *et al.*, *Front. Oncol.*, 2021, **11**, 654921.

40 G. Yang, C. Chen, Y. Zhu, Z. Liu, Y. Xue, S. Zhong, C. Wang, Y. Gao and W. Zhang, *ACS Appl. Mater. Interfaces*, 2019, **11**, 44961–44969.

41 K. Ding, Y. Lu, Z. Nikolovska-Coleska, G. Wang, S. Qiu, S. Shangary, W. Gao, D. Qin, J. Stuckey, K. Krajewski, P. P. Roller and S. Wang, *J. Med. Chem.*, 2006, **49**, 3432–3435.

42 A. Millemaggi and R. J. K. Taylor, *Eur. J. Org Chem.*, 2010, **2010**, 4527–4547.

43 M. Kaur, M. Singh, N. Chadha and Om. Silakari, *Eur. J. Med. Chem.*, 2016, **123**, 858–894.

44 P. Dhokne, A. P. Sakla and N. Shankaraiah, *Eur. J. Med. Chem.*, 2021, **216**, 113334.

45 H. Vakifahmetoglu-Norberg, A. T. Ouchida and E. Norberg, *Biochem. Biophys. Res. Commun.*, 2017, **482**, 426–431.

46 P. Carmeliet and R. Jain, *Nature*, 2000, **407**, 249–257.